Modeling of an anode-supported Ni–YSZ|Ni–ScSZ|ScSZ|LSM–ScSZ multiple layers SOFC cell
Part I. Experiments, model development and validation

Yixiang Shi [a], Ningsheng Cai [a,*], Chen Li [a], Cheng Bao [a], Eric Croiset [b],
Jiqin Qian [c], Qiang Hu [c], Shaorong Wang [c]

[a] *Key Laboratory for Thermal Science and Power Engineering of Ministry of Education, Tsinghua University, Beijing 100084, China*
[b] *Department of Chemical Engineering, University of Waterloo, Waterloo, Ontario N2L 3G1, Canada*
[c] *Shanghai Institute of Ceramics, Chinese Academy of Sciences (SICCAS), 1295 Dingxi Road, Shanghai 200050, China*

Abstract

This paper is the first part of a two-part paper and presents the development, calibration and validation of a two-dimensional isothermal mechanistic model of a composite yttria/scandia-stabilized zirconia anode-supported multiple layers solid oxide fuel cell (Ni–YSZ|Ni–ScSZ|ScSZ|LSM–ScSZ). This model was developed to describe the intricate interdependency among the ionic conduction, electronic conduction, multi-component species transport, electrochemical reaction processes and electrode microstructure for intermediate temperatures operation between 750 and 850 °C. This model takes into account the fact that the electrochemical reactions take place throughout the electrodes and not only at the electrolyte/electrode boundaries. The model was calibrated using experimental polarization curves and then validated by comparing each cell component polarizations (anodic, cathodic and electrolyte) determined from the simulation and from specific experiments using a symmetric cell and EIS measurements.
© 2007 Elsevier B.V. All rights reserved.

Keywords: Intermediate temperature solid oxide fuel cell; ScSZ; Modeling; Experimental validation; Asymmetric and symmetric cells

1. Introduction

A solid oxide fuel cell (SOFC) is an energy conversion device that converts the chemical energy of a fuel directly into electricity [1]. With rising fuel prices and stricter emission control regulations, solid oxide fuel cells become even more attractive due to their high efficiency, low environmental impacts and fuel flexibility.

Electrochemical reactions in SOFC are taking place in a PEN (positive electrode|electrolyte|negative electrode). In order to overcome the problems associated with high temperature operation of state-of-the-art SOFC (around 1273 K), a growing number of researchers are focusing their efforts on intermediate temperature solid oxide fuel cells (IT-SOFCs) for operation between 823 and 1073 K. IT-SOFCs allow for a wider range

of materials and more cost-effective SOFC fabrication methods [2,3]. However, the ionic conductivity of the electrolyte decreases as the operating temperature is lowered. The higher ohmic overpotential at lower operating temperatures could be reduced by using composite ceramic electrolytes that have higher ionic conductivity than conventional YSZ electrolyte, or by adopting an electrode-supported configuration with a thinner electrolyte. One promising configuration for IT-SOFCs is an anode-supported SOFC where a thin electrolyte of thickness in the ranges of 8–15 μm is deposited on a thick anode [4]. In addition, the ionic conductivity and anodic reaction activity could be further improved by adopting a scandia-stabilized zirconia (ScSZ) electrolyte and a Ni/ScSZ composite anode [5,6]. The operation of SOFC involves complex chemical, electrochemical and mass transport processes. The cell performance is strongly affected by several irreversible losses including ohmic losses due to ionic and electronic charge transfer resistances, activation losses due to irreversibility of electrochemical reactions at the three-phase boundary (TPB), and concentration losses due

* Corresponding author. Tel.: +86 1062789955; fax: +86 1062789955.
 E-mail address: cains@mail.tsinghua.edu.cn (N. Cai).

Nomenclature

c	concentration ($\mathrm{mol\,m^{-3}}$)
D	diffusion coefficient ($\mathrm{m^2\,s^{-1}}$)
E	activation energy ($\mathrm{J\,mol^{-1}}$)
E^0	standard cell potential (V)
F	Faraday constant ($96{,}485\,\mathrm{C\,mol^{-1}}$)
i	current density ($\mathrm{A\,m^{-2}}$)
i_{trans}	transfer current density ($\mathrm{A\,m^{-2}}$)
i_0	exchange current density ($\mathrm{A\,m^{-2}}$)
I	current (A)
M_i	molecular weight of species i
n_e	number of electrons participating in the reaction
N	molar flux ($\mathrm{mol\,m^{-2}\,s^{-1}}$)
p	pressure (Pa)
Q	source term for charge balance equations ($\mathrm{A\,m^{-3}}$)
r	average pore size (μm)
R	cell radius (m)
R	gas constant ($8.314\,\mathrm{J\,mol^{-1}\,K^{-1}}$)
R_i	source term for mass balance equations ($\mathrm{kg\,m^{-3}\,s^{-1}}$)
S	cell area ($\mathrm{m^{-2}}$)
S_{TPB}	TPB active area per unit volume ($\mathrm{m^2\,m^{-3}}$)
T	temperature (K)
V	voltage (V)
w_i	mass fraction of species i
x_i	mole fraction of species i

Greek letters

α	transfer coefficient
β	adjustable parameter in exchange current density formulations (see Eqs. (1) and (2)) ($\Omega^{-1}\,\mathrm{m^{-2}}$)
ε	porosity
η	overpotential (V)
ρ	density ($\mathrm{kg\,m^{-3}}$)
σ	conductivity ($\mathrm{S\,m^{-1}}$)
τ	tortuosity

Subscripts

ac	anode chamber
act	active layer
an	anode
avg	average
ca	cathode
cc	cathode chamber
elec	electronic
electrolyte	electrolyte
inter	interface
ion	ionic
leak	leak
op	open circuit
p	pore
ref	reference
sp	support layer
symmetry	axis of symmetry
th	theoretical

to mass transport resistance in the electrode, especially for thick anodes as in an anode-supported SOFC [7]. In reality, leak overpotential associated with parasitic loss due to current leakage, gas crossover, and unwanted side reactions must also be considered. High SOFC performance relies on optimal electrochemical reactions and mass transport processes. Since experimental studies on SOFC are expensive, time-consuming and labor-intensive, quantitative mechanistic models for the cell PEN structure are essential for SOFC technology development. A validated mechanistic model offers not only a means to better understand the complex physical phenomena governing fuel cell performance that are not readily accessible experimentally; they also can be useful design tools.

In recent years, several SOFC models have been developed to study reactions and transport phenomena within the PEN structure. These models differ widely in terms of their complexity and comprehensiveness.

Tanner et al. [8] developed an empirical model based on the works of McDougall [9] to calculate the effective charge transfer resistance of an electrode as a function of intrinsic charge transfer resistance, ionic conductivity of the electrolyte and electrode thickness. In order to predict the concentration polarization in detail, Virkar et al. [10] and Kim et al. [11] considered porous media gas phase transport processes based on Fick's model to predict concentration overpotentials, and used Tanner's method to calculate activation overpotentials. Although those empirical models could predict the cell performance conveniently they are limited to particular cells and cannot describe in detail the effects of operating and design parameters.

One-dimensional PEN models adopt conservation laws to describe the reaction and transport processes occurring within the cell and could be used to identify the effects of each layer in the PEN. Costamagna [12,13] developed a one-dimensional continuum micro-scale models in which the effective properties were estimated based on statistical properties of random packing systems of binary spherical particles and percolation theory. Chan et al. [14,15] adapted this model to consider the effects of concentration overpotential by taking the molecular and Knudsen diffusion into account. These models were used for detailed simulation of only one electrode (anode or cathode). These continuum micro-scale models were extended to the whole PEN by Nam and Jeon [16] and Shi and Cai [17] to build a bridge connecting micro-scale to macro-scale models. However, a one-dimensional PEN model could only represent the parameter variation along the direction of the PEN thickness. For instance, they could not be used to calculate the distribution of the electric current path inside the PEN. In addition, such one-dimensional models cannot model the effects of asymmetric electrodes, which were thus omitted. Therefore, a comprehensive multi-dimensional model is necessary when attempting to simulate the intricate interdependency among the ionic conduction, electronic conduction, gas transport phenomena, and electrochemical processes. Numerous multi-dimensional SOFC models exist in the open literature with varying sets of assumptions depending on the objectives of the simulation [18–23]. However, in order to simplify the calculation, these published multi-dimensional models treated the reaction zone as boundary

conditions. This is not consistent with the fact that the reaction zone layer in an SOFC is spread into the electrode to some distance from the electrode/electrolyte interface [14,15,17,24]. In addition, since the electrode microstructure has a direct impact on the cell performance [12], including micro structural characteristics in the model can provide insights that relate microstructure to performance. Such a model would be particularly useful for cell design and optimization. Unfortunately, few of the existing multi-dimensional PEN models relate the electrode microstructure to the cell electrochemical reaction characteristics.

Furthermore, for a given mathematic model, although most of the model parameters are determined from experiments or from literature, others are only estimates. Some of the parameters are adjusted to ensure good agreement between the model results and the experimental data, for examples exchange current density and tortuosity [17]. The uncertainty in the estimated parameter will surely influence the model reliability and accuracy. The more the parameters are determined independently through experiments or characterization techniques, the more robust the model.

In this paper, an isothermal mechanistic model that considers the cell microstructure and reactions to occur over the whole electrode was calibrated and validated using experimental data obtained on a button cell consisting of Ni–YSZ|Ni–ScSZ|ScSZ|LSM–ScSZ multiple layers. This model has already been presented in detail in a previous paper [25]. However, contrary to the model presented earlier on, the present model can accommodate multi-components. In addition, an important feature of the validation process presented here is that the model is not only validated using the overall polarization curve as it is usually done in the literature, but it is also validated by considering overall losses over each cell component, namely anode, cathode and electrolyte, and thereafter referred to as anodic, cathodic and electrolyte overpotentials, respectively. Note that in the "electrolyte" overpotential we also include the loss due to contact resistance between the electrodes and electrolyte. The methods to isolate each cell component over-

potential from experiments and from simulation are described in Sections 5.2 and 5.3, respectively.

2. PEN structure and experimental apparatus

2.1. Anode-supported SOFC PEN structure

Fig. 1 illustrates the PEN structure of the anode-supported button cell. The PEN used in this paper consists of a Ni/YSZ anode support layer (680 μm), a Ni/ScSZ anode active interlayer (15 μm), a ScSZ thin-film electrolyte layer (20 μm) and a LSM/ScSZ cathode layer (15 μm). Except for the cathode layer which has a diameter of 1.4 cm, all other layers have a diameter of 2.6 cm. The electrodes are composed of electronic and ionic conductor particles and are porous to facilitate the transport of fuel and oxidant from the gas channel to the three phase boundaries where the electrochemical reactions occur. The electrolyte is dense to keep the air and fuel gases separated and thus allowing for an oxygen concentration difference between the anode and the cathode. Oxygen ions are produced at the TPB sites near the cathode/electrolyte interface, and are transported by a solid-state migration mechanism through the electrolyte to the anode/electrolyte interface, where oxygen ions react with the fuel. Product molecules are then transported back to the fuel channel through the pores.

2.2. Cell preparation

Commercial NiO (Inco Ltd., Canada) was used with 8 mol% yttria-stabilized ZrO_2 (YSZ, TOSOH, Japan) powder for preparing the support layer and with scandia-stabilized zirconia, $Zr_{0.89}Sc_{0.1}Ce_{0.01}O_{2-x}$ (ScSZ, Daiichi Kigenso Kagaku Kogyo, Japan), for the anode active layer. The ratio of the mixtures (NiO–YSZ and NiO–ScSZ) was 50 wt% NiO and 50 wt%-stabilized zirconia. The ScSZ powder was also used to prepare the electrolyte film.

The slurries for the tape casting process were prepared by a ball milling process that included two steps. In the first step, all
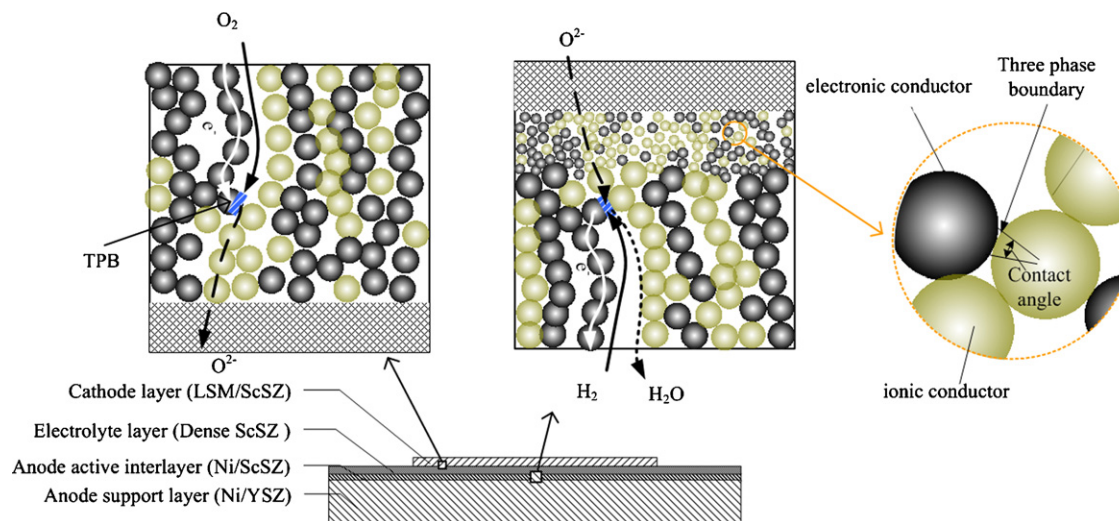

Fig. 1. Schematic representation of the anode-supported SOFC button cell used in this study.

the above-mentioned ceramic powders were homogenized in a planetary mill for 2 h with dispersant in a mixture of methyl ethyl ketone (MEK) and ethanol (EtOH). To form sufficient porosity in the anode support and active layers, a certain amount of rice starch was added as pore former to the mixture of NiO–YSZ and NiO–ScSZ. Other organic additives, such as polyvinyl butyral (PVB) and a mixture of polyethylene glycol (PEG) and dibutyl *o*-phthalate (DOP) were added as binder and plasticizer, respectively, in adequate quantity and proportion, and then milled for another 2 h.

Prior to tape casting, the slurries were vacuum pumped for about 2 min in order to remove any remaining air. The ScSZ film was casted first onto the glass plate by a "doctor blade" method and allowed to dry in air for several minutes; the anode functional and active layers were prepared similarly. After drying overnight at room temperature, the multilayer green tape was detached and co-sintered at 1400 °C in air for 4 h.

The LSM (Inframat advanced materials, USA) and ScSZ powders in a mass ratio of 50:50 were mixed in a planetary mill with ethanol for 3 h to ensure random distribution of each phase. The dried mixture was subsequently grounded in an agate mortar with ethyl cellulose and terpineol to prepare the paste, which was screen-printed onto the sintered ScSZ layer and sintered at 1200 °C for 3 h to form the cathode.

2.3. Test setup

Fig. 2 shows the schematic representation of the test station used for evaluating the performance of the button cell test.

The cell was located between two alumina tubes. Pt wires were used as voltage and current probe. The Pt mesh was used as the cathode current collector and was fixed to the porous cathode with platinum paste. The porous Ni felt was used as the anode current collector and was fixed to the anode support layer with platinum paste. Before testing, the anode was fully reduced at 850 °C in a 20:80 $H_2:N_2$ mixture (total flowrate of 50 sccm). During the actual tests, H_2 mixtures were humidified at room temperature (30 °C, 4% H_2O) and used as fuel; oxygen or air was used as oxidant. The flow rates of fuel and oxidant were both kept at 50 sccm. The polarization curves were measured using four-probe method with an Electrochemical Workstation (IM6e, Zahner-Elektrik GmbH, Germany) for temperatures ranging from 700 to 850 °C. The measurements were initiated after the system was stable under a constant voltage of 0.7 V for 30 min. Electrochemical impedance spectroscopy (EIS) was performed using an amplitude of 10 mV over the frequency range 0.1 Hz to 100 kHz. The ohmic resistance of the whole cell was estimated from the high frequency intercept of the impedance curves.

After the cell tests, the cell surface and cross-section, as well as the elemental distribution, were characterized by scanning electronic microscope (SEM) and energy dispersive spectrometer (EDS) using an electron probe microanalyzer (JSM-6460, JEOL, Japan). The actual thickness of the cell components were also determined using SEM. The porosity and tortuosity of the different layers before and after the cell tests were determined using mercury porosimetry (AutoPore IV 9510, Micromeritics, USA) and image processing.
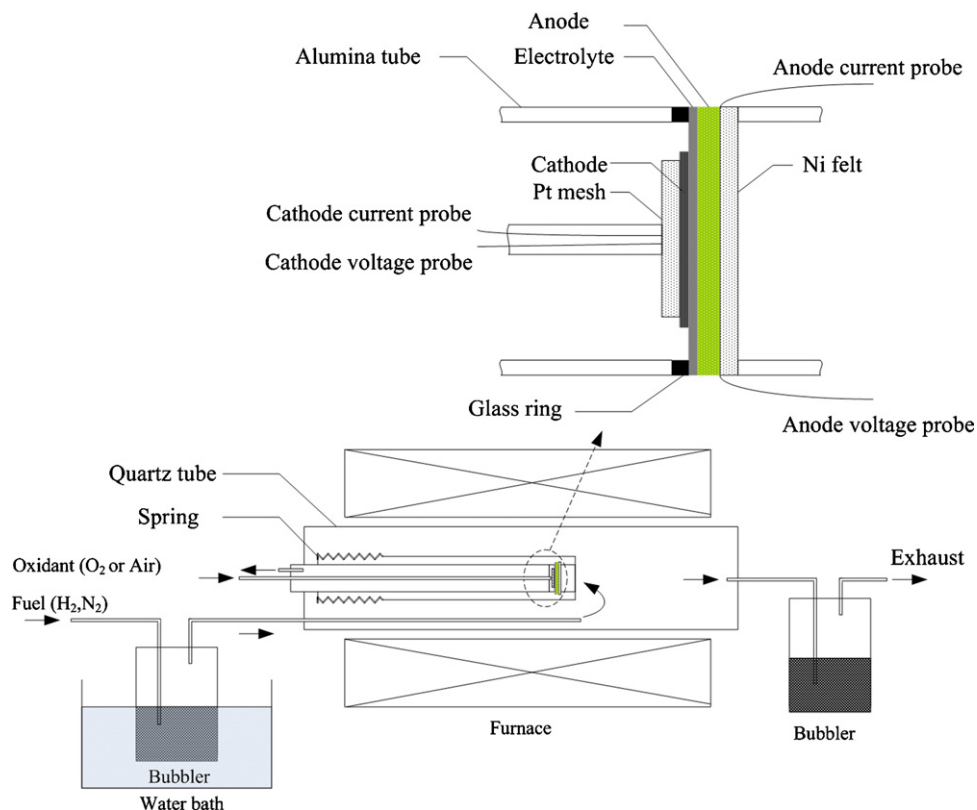

Fig. 2. Schematic representation of the test setup.

3. Model development

3.1. Model assumptions and model geometry

The assumptions made in this model are the following:

(1) The PEN operates at steady state.
(2) All gas mixtures are considered as ideal gases.
(3) The reaction active sites are assumed to be uniformly distributed in each electrode layer. The two conducting phases (electronic and ionic) are considered to be continuous and homogeneous in each layer.
(4) The temperature is uniform in the PEN, thus the model is assumed isothermal and all physical properties are evaluated at a fixed cell temperature.
(5) Convection flux is neglected in the porous electrode compared to diffusion. Pressure gradients in the porous electrode are also neglected.
(6) The boundary conditions for potential and species concentrations are assumed uniform at the electrode/gas channel interface.

In addition, it should be noted that the reaction zone may not be restricted to the anode active interlayer but may spread into the anode support layer, especially if the active interlayer is relatively thin. Thus, the governing equations for the anode-supported layer are the same as for the anode active layer, although some parameters may be different.

Due to symmetry, a two-dimensional axial symmetry coordinate is adopted, as shown in Fig. 3. In this figure the labeling of the calculation domains and boundaries are also shown. The type of boundary conditions for each domain will be described later in the paper.

With the above assumptions and model geometry, the SOFC PEN model is formulated using charge balances, mass balances together with electrochemical reaction kinetics, as described in the following sections.

3.2. Governing equations

Most of the governing equations have been presented in detail in a previous paper [25]. Only the differences between the present model and the model used in [25], as well as some additional information are highlighted here:

- In the present model surface diffusion has not been taken into account.
- Material balances in the present model accommodate more than two components using the dusty gas model [28].
- The expression of anodic exchange current density (both anode support layer and anode active layer) is kept the same as in Ref. [25]:

$$i_{0,\text{an}} = \frac{\beta_{\text{an}} RT}{3F} \left(\frac{c_{\text{H}_2}}{c_{\text{ref,H}_2}} \right) \exp\left(-\frac{E_{\text{act,an}}}{RT} \right) (p_{\text{O}_2,\text{an}})^{0.133} \quad (1)$$

where $i_{0,\text{an}}$ is the anodic exchange current density, $c_{\text{ref,H}_2}$ is the hydrogen concentration in the reference case and $p_{\text{O}_2,\text{an}}$ is the oxygen partial pressure at the anode. For the support layer we kept the values found in Ref. [27], that is $E_{\text{act,an}} = 120{,}000\,\text{J mol}^{-1}$ and $\beta_{\text{an}} = 6.17 \times 10^{11}\,\Omega^{-1}\,\text{m}^{-2}$. For the active layer, $E_{\text{act,an}}$ is kept constant at $120{,}000\,\text{J mol}^{-1}$ and β_{an} is treated as an adjustable parameter to fit the experimental data.

- The cathodic exchange current density is expressed in a different form than in Ref. [25]. It is determined using the expression found in Costamagna et al. [27]:

$$i_{0,\text{ca}} = \frac{\beta_{\text{ca}} RT}{4F} \exp\left(-\frac{E_{\text{act,ca}}}{RT} \right) (p_{\text{O}_2,\text{ca}})^{0.25} \quad (2)$$

where $i_{0,\text{ca}}$ is the cathodic exchange current density and $p_{\text{O}_2,\text{an}}$ is the oxygen partial pressure at the cathode. $E_{\text{act,ca}}$ is kept constant at $130{,}000\,\text{J mol}^{-1}$ while β_{ca} is also treated as an adjustable parameter, similar to β_{an}.

- η is the local overpotential defined as

$$\eta = V_{\text{elec}} - V_{\text{ion}} - V_{\text{ref}} \quad (3)$$

where V_{ref} is the relative potential difference between the electronic and ionic conductors at a reference state.

- Open-circuit state was chosen as the reference state here. By setting $V_{\text{ref,an}}$ to zero, the cathode reference potential $V_{\text{ref,ca}}$ will be the open circuit voltage. However, it should be noted that the experimental open circuit voltage values are typically slightly less than the theoretical values. This difference is due to slight gas leaks in a single cell test and thus, this potential
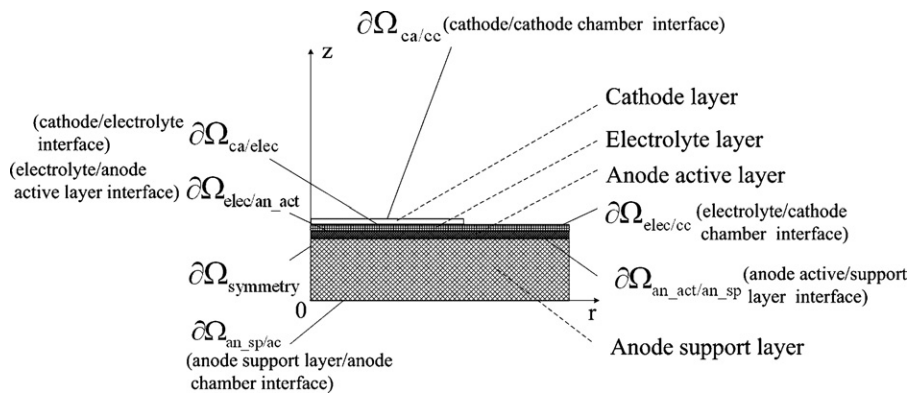

Fig. 3. Two-dimensional axisymetrical model geometry.

difference is called "leak overpotential", denoted as η_{leak} and kept constant in this study. The cathode reference potential can thus be formulated as

$$V_{\text{ref,ca}} = V_{\text{op}} + \underbrace{V_{\text{ref,an}}}_{=0} = V_{\text{op,th}} - \eta_{\text{leak}}$$

$$= E^0 - \frac{RT}{2F} \ln\left(\frac{p_{\text{O}_2,\text{ca}}^{0.5} p_{\text{H}_2,\text{an}}}{p_{\text{H}_2\text{O},\text{an}}}\right) - \eta_{\text{leak}} \quad (4)$$

where V_{op} denotes the actual cell open circuit voltage, $V_{\text{op,th}}$ is the theoretical open circuit voltage, E^0 is the standard cell potential, and $p_{\text{H}_2,\text{an}}$ and $p_{\text{H}_2\text{O},\text{an}}$ are the partial pressures of hydrogen and water at the anode, respectively.

The governing equations for the electrode charge balances are summarized in the following equations (see nomenclature for the definition of each term and Ref. [25] for more details).

- Ionic charge at the cathode:

$$-\nabla(\sigma_{\text{ion,ca}}^{\text{eff}} \nabla V_{\text{ion,ca}})$$
$$= Q_{\text{ion,ca}} = -i_{0,\text{ca}} S_{\text{TPB,ca}}$$
$$\times \left(\frac{c_{\text{O}_2}^{\text{TPB}}}{c_{\text{O}_2}^{\text{bulk}}} \exp\left(\frac{\alpha n_e F(V_{\text{elec,ca}} - V_{\text{ion,ca}} - V_{\text{ref,ca}})}{RT}\right) \right.$$
$$\left. - \exp\left(-\frac{(1-\alpha)n_e F(V_{\text{elec,ca}} - V_{\text{ion,ca}} - V_{\text{ref,ca}})}{RT}\right) \right) \quad (5)$$

- Electronic charge at the cathode:

$$-\nabla(\sigma_{\text{elec,ca}}^{\text{eff}} \nabla V_{\text{elec,ca}}) = Q_{\text{elec,ca}} = -Q_{\text{ion,ca}} \quad (6)$$

- Ionic charge at the anode:

$$-\nabla(\sigma_{\text{ion,an}}^{\text{eff}} \nabla V_{\text{ion,an}})$$
$$= Q_{\text{ion,an}} = i_{0,\text{an}} S_{\text{TPB,an}}$$
$$\times \left(\frac{c_{\text{H}_2}^{\text{TPB}}}{c_{\text{H}_2}^{\text{bulk}}} \exp\left(\frac{\alpha n_e F(V_{\text{elec,an}} - V_{\text{ion,an}} - V_{\text{ref,an}})}{RT}\right) \right.$$
$$\left. - \frac{c_{\text{H}_2\text{O}}^{\text{TPB}}}{c_{\text{H}_2\text{O}}^{\text{bulk}}} \exp\left(-\frac{(1-\alpha)n_e F(V_{\text{elec,an}} - V_{\text{ion,an}} - V_{\text{ref,an}})}{RT}\right) \right) \quad (7)$$

- Electronic charge at the anode:

$$-\nabla(\sigma_{\text{elec,an}}^{\text{eff}} \nabla V_{\text{elec,an}}) = Q_{\text{elec,an}} = -Q_{\text{ion,an}} \quad (8)$$

The governing equations for the electrode mass balances are summarized as follows:

- Mass balance at the anode:

$$-\nabla\left(\rho w_{\text{H}_2} \sum_{j=1}^{n} \tilde{D}_{\text{H}_2,j} \nabla x_j\right) = \frac{-i_{\text{trans,an}} S_{\text{TPB,an}} M_{\text{H}_2}}{2F} \quad (9)$$

Table 1
Boundary conditions

Boundary	Ionic charge	Electronic charge	Mass balance
$\partial\Omega_{\text{ca/cc}}$	Insulation	$V_{\text{cell,ca}}$	$w_{\text{O}_2,\text{bulk,ca}}$, $w_{\text{N}_2,\text{bulk,ca}}$
$\partial\Omega_{\text{elec/cc}}$	Insulation	Insulation	Insulation
$\partial\Omega_{\text{ca/elec}}$	Continuity	Insulation	Insulation
$\partial\Omega_{\text{elec/an\_act}}$	Continuity	Insulation	Insulation
$\partial\Omega_{\text{an\_act/an\_sp}}$	Continuity	Continuity	Continuity
$\partial\Omega_{\text{an\_sp/fc}}$	Insulation	$V_{\text{cell,an}}$	$w_{\text{H}_2,\text{bulk,an}}$, $w_{\text{H}_2\text{O},\text{bulk,an}}$, $w_{\text{N}_2,\text{bulk,an}}$
$\partial\Omega_{\text{symmetry}}$	Symmetry	Symmetry	Symmetry
Others	Insulation	Insulation	Insulation

$$-\nabla\left(\rho w_{\text{H}_2\text{O}} \sum_{j=1}^{n} \tilde{D}_{\text{H}_2\text{O},j} \nabla x_j\right) = \frac{-i_{\text{trans,an}} S_{\text{TPB,an}} M_{\text{H}_2\text{O}}}{2F} \quad (10)$$

- Mass balance at the cathode:

$$-\nabla\left(\rho w_{\text{O}_2} \sum_{j=1}^{n} \tilde{D}_{\text{O}_2,j} \nabla x_j\right) = \frac{-i_{\text{trans,an}} S_{\text{TPB,an}} M_{\text{O}_2}}{4F} \quad (11)$$

3.3. Boundary conditions

In order to solve the system of coupled partial differential equations for charge and mass balances, the boundary conditions of all outer interfaces are specified in Table 1 (refer also to Fig. 3).

The difference between $V_{\text{cell,ca}}$ and $V_{\text{cell,an}}$ is the cell voltage used in the calculation. Here, we chose $V_{\text{cell,an}} = 0$. $w_{i,\text{bulk}}$ in the table is the mass fraction of species i in the fuel/air channel.

The boundary conditions "Insulation" and "Symmetry" both mean that the partial derivative of the variable at the boundary is zero. The difference is that for "Symmetry" there is a flux through the boundary, while for "Insulation" there is none.

3.4. Solution method

The problem was solved for a given cell voltage. The outputs of the model are the distributions of current density and species concentrations. The calculations were performed using the finite element commercial software COMSOL MULTIPHSICS®, Version 3.2.

From the current density distribution, the average current density was calculated as

$$i_{\text{avg}} = \frac{I_{\text{total}}}{S} = \frac{1}{R^2} \int_0^R 2r i_{\text{local}} \, dr \quad (12)$$

where i_{local} is the local current density and R is the radius of the interface based here on the cathode area.

In order to generate a complete polarization curve, the calculation was performed over a range of cell voltages, for which a corresponding average current density was determined.

4. Model calibration

The process of model calibration involves the following two steps: (1) evaluation of model parameters such as microstructure properties and kinetic parameters; (2) model calibration for a "base case" (here humidified H_2 with air at 1 atm for temperatures between 750 and 850 °C). Ideally, all model parameters should be determined independently from literature data or from characterization techniques. Unfortunately, this is not possible for some parameters (e.g. leak overpotential, an intrinsic parameter of the experimental setup), which then must be estimated by tuning their value to fit the experimental data during the calibration step. However, once all model parameters are determined, they were not changed when simulating other cases as in the final step of the model validation procedure.

4.1. Model parameters

Except for the exchange current density, which expression was found in Costamagna et al. [26], all other kinetic parameters were taken from the work of Nagata et al. [27]. This section describes then how the model parameters related to the microstructure of the different cell layers were estimated. Those parameters are: layer thickness, ionic conductivities and, in the case of the electrodes, pore size, tortuosity and electronic conductivities.

A picture showing the appearance and dimension of the button cell used in this study is shown in Fig. 4. The thickness of each layer was determined from SEM micrographs of the cell cross-section, as shown in Fig. 5.

The pore size and porosity of the cell were characterized using mercury porosimetry. The mean pore diameter and porosity were found to be 0.46 μm and 0.364, respectively. It is very difficult to differentiate the pore size and porosity of anode active layer and cathode layer from that of the anode support layer since they are very thin compared to the anode support layer. Actually, the values of pore size and porosity determined from mercury porosimetry are essentially characteristics of the anode support
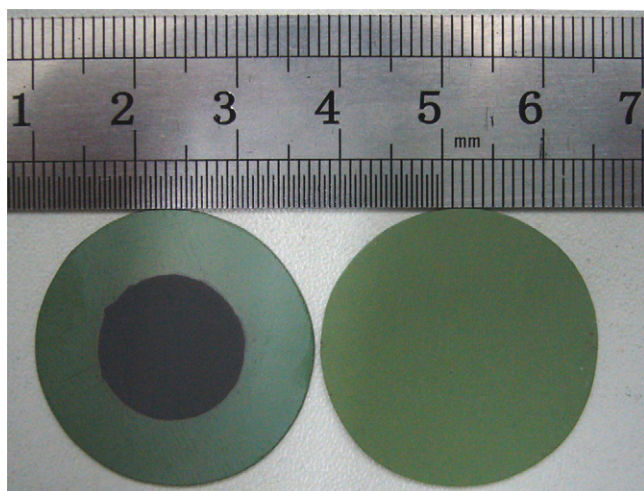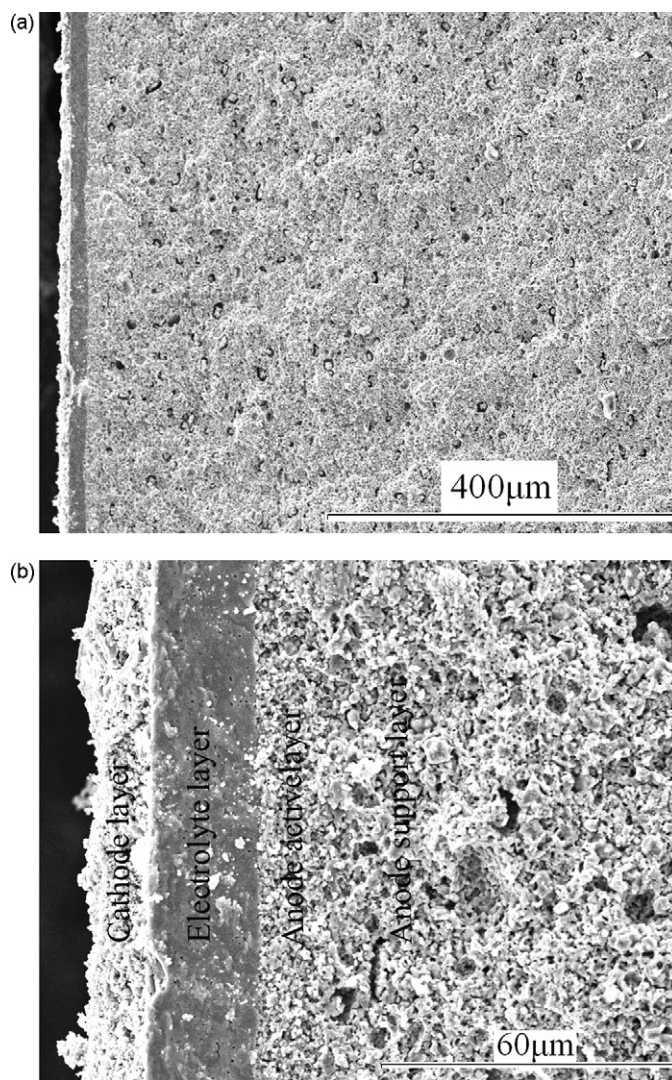

Fig. 5. SEM micrographs after tests: (a) overall cell cross-section and (b) detailed view of cell cross-section.

Fig. 4. Photograph of the button cell used in the experiment. Left: cathode side, right: anode side.

layer. Thus, an image processing software (ImageJ V1.34) was used to determine the pore size and porosity of each layer from SEM images based on quantitative stereology [28,29]. It should be noted that the porosity and pore size from image analysis were only used to determine their relative value compared to that of the anode support layer. The values used in the model were adjusted accordingly, based on the values of pore size and porosity of the anode support layer determined from mercury porosimetry.

At first, the SEM images were contrasted and filtered by the ImageJ software. After thresholding, the binarized images were used to determine the porosity and the pore size distributions. According to stereological assumptions, the calculated porosity is equal to the pore volume proportion [28]. An "equivalent pore radius" [29] was used to quantify the pore size since the shape of the pores varies significantly. To reduce measuring errors, measurements were performed five times at different position of each layer. Fig. 6 illustrates a comparison between pore size distribution obtained by image analysis and mercury porosimetry. The porosity, average pore area and equivalent radius of anode

Table 2
Porosity, average pore area and equivalent radius evaluated by image analysis

Sample number	Anode support layer			Anode active layer			Cathode layer		
	Porosity	Average pore area (m^2)	Equivalent pore radius (μm)	Porosity	Average pore area (m^2)	Equivalent pore radius (μm)	Porosity	Average pore area (m^2)	Equivalent pore radius (μm)
1	0.265	6.92E−13	0.47	0.261	2.83E−13	0.30	0.282	4.94E−13	0.40
2	0.291	8.31E−13	0.51	0.277	2.71E−13	0.29	0.274	4.25E−13	0.37
3	0.248	6.38E−13	0.45	0.271	3.27E−13	0.32	0.272	5.79E−13	0.43
4	0.299	8.29E−13	0.51	0.278	2.77E−13	0.30	0.252	5.27E−13	0.41
5	0.267	6.58E−13	0.46	0.291	3.39E−13	0.33	0.253	5.39E−13	0.41
Average	0.274	7.30E−13	0.48	0.276	2.99E−13	0.31	0.267	5.13E−13	0.40

active layer, anode support layer and cathode layer evaluated from image processing are shown in Table 2.

The results show that the pore size distribution of the anode support layer obtained from image analysis is somewhat different from that obtained from mercury porosimetry. The porosity determined from image analysis (ca. 0.27) is lower than that from mercury porosimetry (0.365). This is not too much an issue here, because we are only interested in knowing the relative values of porosity and pore size of the anode active layer and cathode layer, compared to that of the anode support layer.

According to Table 2, the porosity of the three layers can be assumed identical. The average pore radius of the cathode layer (0.40 μm) is considered close enough to the value of that of the anode support layer (0.48 μm) that we considered them to be the same. However, the average pore radius of the anode active layer (0.31 μm) is assumed to be 1.5 times smaller than that of the anode support layer.

Particles in the electrode consist of agglomerates of different sizes before sintering. To simplify the calculation, the mean particle radius of the ionic conductor is assumed to be equal to that of the electronic conductor within the same layer [12]. The relationship between the mean particle radius, r_{elec}, and mean pore size, r_p, is as follows [16]:

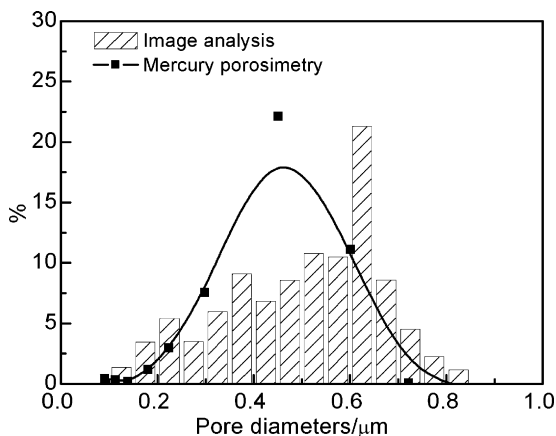$$r_{elec} = \frac{3(1 - \varepsilon)r_p}{2\varepsilon} \qquad (13)$$

Fig. 6. Pore size distribution of anode support layer obtained by image analysis and mercury porosimetry.

Table 3
Material conductivities

Material	Conductivity ($S\,m^{-1}$)
Ionic conductor	
ScSZ	$6.92E4 \exp(-9681/T)$[a]
YSZ	$3.34E4 \exp(-10300/T)$ [30]
Electronic conductor	
LSM	$4.2E7/T \exp(-1150/T)$ [30]
Ni	$3.27E6 - 1065.3T$[16]
Equivalent ionic conductivity of electrolyte layer	$0.002T - 1.4483$[a]

[a] Curve fitting according to the experimental data.

Table 3 lists the conductivities of ionic conductor, electronic conductor as well as the equivalent conductivity of the electrolyte layer (i.e. when the whole conductivity of the cell is reduced to that of the electrolyte layer), which was determined by EIS spectra at open circuit state.

4.2. Model calibration

During model calibration, a few parameters have been allowed to vary and be tuned to best fit the experimental data under one set of operating conditions referred to as "base case". The operating conditions of the base case are listed in Table 4. The parameters to be tuned were the leak overpotential, cathode and anode tortuosities, and kinetics related parameters since the material used in the active anode layer is different from that of Costamagna and Honegger [26] and Nagata et al. [27], whose kinetic parameters were used as a starting point. The model parameters tuned in the base case are summarized in Table 5. The cell performance at three temperatures (750/800/850 °C) were calculated and measured experimentally while the fuel was humidified at a constant temperature of 30 °C.

Table 4
Operation conditions in the base case

Parameters	Value
Pressure, p (Pa)	101,325
Temperature, T (°C)	750/800/850
Fuel composition	96% H_2 and 4% H_2O (saturated hydrogen at 30 °C)
Oxidant composition	21% O_2 and 79% N_2

Table 5
Tuned model parameters

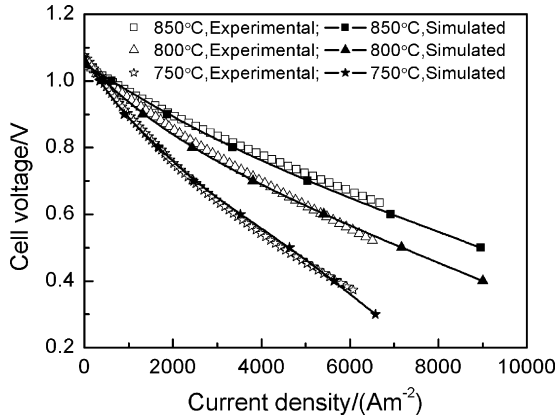| Parameter	Value
Leak overpotential, η_{leak} (V)	0.03
β_{an} in Eq. (1) (Ω^{-1} m^{-2})	6.8E12
β_{ca} in Eq. (2) (Ω^{-1} m^{-2})	5.8E10
Anode tortuosity	16.5
Cathode tortuosity	3

Fig. 7. Comparison between modeling and experimental data for the base case.

The polarization curves shown in Fig. 7 show that the experimental and modeling results at different temperatures agree well. Obviously, the operating temperature significantly affects the cell performance. Although the open circuit voltage decreases when increasing temperature, cell performance at higher temperatures is better because not only are the electrochemical reactions and mass transport faster, but also the ionic conductivity of the electrolyte is considerably higher.

5. Model validation

The experimental polarization curves represent only the gross behavior of each component of the single button cell. The model was therefore validated by comparing each cell component polarization loss (anodic, cathodic and electrolyte) obtained experimentally and through simulation. Note that to determine experimentally the various polarizations, as explained in the next section, a different set of experiments using a different cell was used.

5.1. Determination of each cell component polarization from experiments

To determine each polarization loss experimentally, a symmetric cell, shown in Fig. 8, was used to estimate first the cathodic polarization. The symmetric cathode was printed on a commercial ScSZ film in the same way as described previously for the single button cell. The total ohmic resistance was measured by EIS tests on the symmetric cell from the high frequency intercept of the impedance curves. By subtracting the ohmic polarization from the measured polarization and then dividing by two, the cathodic polarization was determined. The anodic
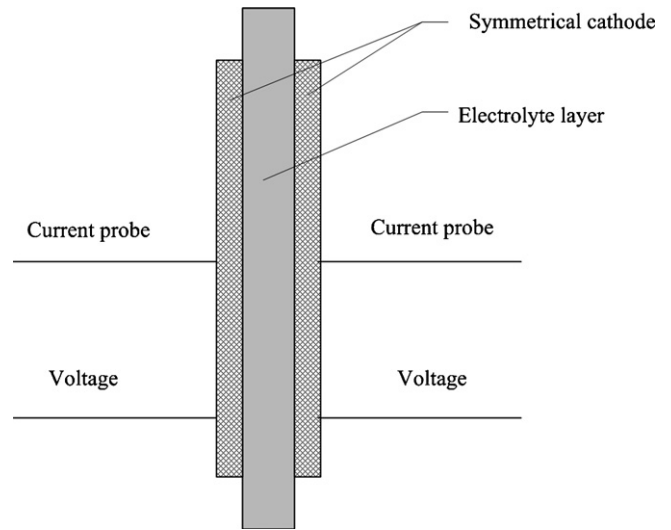

Fig. 8. Symmetric cell used to determine the cathodic polarization.

polarization was then estimated by subtracting the ohmic polarization, cathodic polarization and leak overpotential from the total polarization of the single cell. The symmetric cell used for polarization measurement should be carefully prepared to make sure that the cathode in the symmetric cell and the one in single button cell were identical. Through EIS measurements at high frequency, considering that the electrodes are good conductors, it is reasonable to assume that the resistance thus determined (high frequency intercept of the impedance curves) include essentially the contact and electrolyte ohmic resistances. The polarization due to both contact and electrolyte resistances was then calculated from the value of the resistance determined from EIS measurement.

5.2. Determination of each cell component polarization from simulations

The local overpotential was defined in Eq. (3). The cathodic and anodic overpotentials were calculated as

$$\eta_{an} = |(V_{elec}|_{an-sp/ac} - V_{ion}|_{electrolyte/an-act}) - V_{ref,an}| \quad (14)$$

$$\eta_{ca} = |(V_{elec}|_{ca/ac} - V_{ion}|_{electrolyte/ca}) - V_{ref,ca}| \quad (15)$$

The ohmic polarization was calculated as

$$\eta_{electrolyte} = (V_{ion}|_{electrolyte/ca} - V_{ion}|_{electrolyte/an\_act}) \quad (16)$$

Recall that, as defined in Section 1 and as seen in Eq. (16), the "electrolyte" overpotential ($\eta_{electrolyte}$) also includes the loss due to contact resistance between the electrodes and the electrolyte.

The total cell overpotential was then calculated as

$$\eta_{total} = \eta_{an} + \eta_{ca} + \eta_{electrolyte} + \eta_{leak} \quad (17)$$

5.3. Comparison experiments/simulations

It can be seen from Fig. 9 that the calculated total overpotential and the overpotential of each component all agree well with the experimental data in the base case at 800 °C.
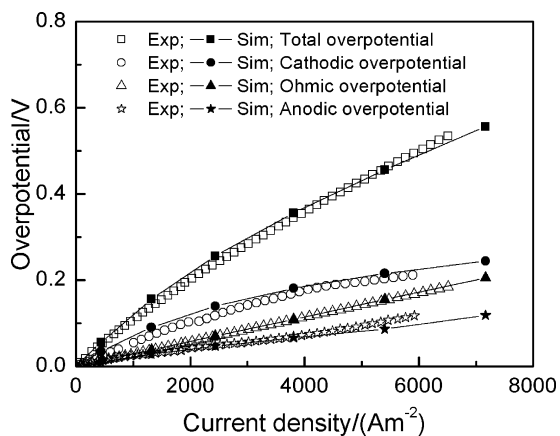
Fig. 9. Modeling and experimental results of cell overpotentials.

Fig. 11. Calculated and experimental cathodic overpotential at 750, 800 and 850 °C.

As a mathematical trick, if the source terms of the anode and cathode mass balance equations (Eqs. (9)–(11)) are set to zero, the fuel and oxidant concentrations are uniform throughout the electrodes and equal to the concentrations at the electrode/gas chamber interfaces. In this way, the effects of concentration overpotential could be separated. The simulated detailed contributions of each PEN component to cell overpotential (including concentration overpotential) in the base case at 800 °C are shown in Fig. 10.

It is seen from Fig. 10 that the cathodic activation overpotential and the ohmic overpotential dominate for SOFC operation at 800 °C with air and current density below 10,000 A m^{-2}. The activation polarization of the anode is between 40 and 50% of the cathodic activation overpotential. The cathodic concentration polarization in the base case can be neglected because the cathode is thin enough. The anodic concentration polarization is more important than the cathodic one because of the thick anode. Nonetheless, compared to the anodic, cathodic and ohmic losses, the anodic concentration overpotential remains small (less than 5% of total overpotential) in the base case for our button cell. However, the anodic concentration overpotential increases with the current density.

The effect of temperature on the cathodic overpotentials is shown in Fig. 11 for temperatures between 750 and 850 °C.
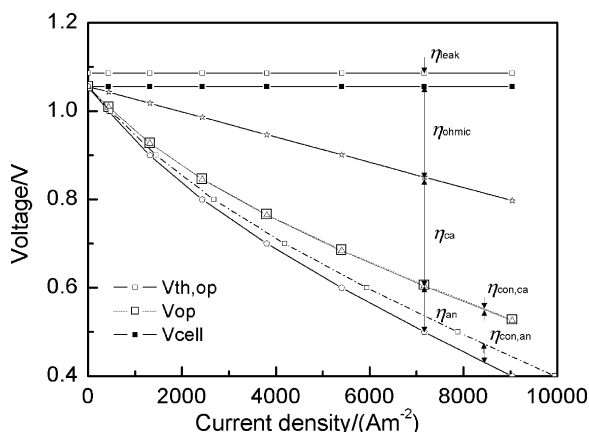
Both calculated and experimental results show that the operating temperature significantly affects the cathodic overpotential, which increases as the temperature decreases, as expected. In addition, this figure shows that the model is valid over a wide range of temperatures, but somewhat understimates the cathodic polarization at 850 °C, and somewhat overestimates the cathodic polarization at 750 and 800 °C.

6. Conclusions

A two-dimensional isothermal mechanistic PEN model of an anode-supported solid oxide fuel cell was developed to describe the intricate interdependency among the ionic conduction, electronic conduction, multi-component species transport, electrochemical reaction processes and electrode microstructure. The model was calibrated and validated for an IT-SOFC button cell, comprised of Ni–YSZ|Ni–ScSZ|ScSZ|LSM–ScSZ multiple layers. Five parameters were tuned, namely leak overpotential, pre-exponential factors of anodic and cathodic electrochemical kinetic expressions (the β's) and anodic and cathodic tortuosities. Tuning of these parameters led to a good match between the overall polarization curves obtained experimentally and from simulation for humidified hydrogen (4% H$_2$O) operating at temperatures between 750 and 850 °C. The model was then validated by comparing each cell component polarizations (anodic, cathodic and electrolyte) determined from the simulation and from specific experiments using a symmetric cell and EIS measurements. This validation process showed that the model was able to describe accurately each polarization. In part II of this two-part paper further validation is carried out over a wider range of operating conditions (e.g. different fuel and oxidant compositions) and the model is used to further discuss the effect of cell microstructure on cell performance.

Fig. 10. Contributions of each PEN component to cell overpotential (simulation results).

References

[1] J. Larminie, A. Dicks, Fuel Cell Systems Explained, Wiley & Sons, Chichester, 2000, pp. 1–3.

[2] Y. Jiang, A.V. Virkar, Fuel composition and diluent effect on gas transport and performance of anode-supported SOFCs, J. Electrochem. Soc. 150 (2003) A942–A951.

[3] A.V. Virkar, Low-temperature, anode-supported high power density solid oxide fuel cells with nanostructured electrodes, Contract No.: AC26-99FT40713, 2003.

[4] J. Yuan, B. Sundén, Analysis of intermediate temperature solid oxide fuel cell transport processes and performance, Trans. ASME J. Heat Transfer 127 (2005) 1380–1390.

[5] A. Gunji, C. Wenb, J. Otomo, T. Kobayashi, K. Ukai, Y. Mizutani, H. Takahashi, Carbon deposition behaviour on Ni–ScSZ anodes for internal reforming solid oxide fuel cells, J. Power Sources 131 (2004) 285–288.

[6] H. Kishimoto, K. Yamaji, T. Horita, Y.-P. Xiong, N. Sakai, M.E. Brito, H. Yokokawa, Reaction process in the Ni–ScSZ anode for hydrocarbon fueled SOFCs, J. Electrochem. Soc. 153 (2006) A982–A988.

[7] H. Yakabe, M. Hishinuma, M. Uratani, Y. Matsuzaki, I. Yasuda, Evaluation and modeling of performance of anode-supported solid oxide fuel cell, J. Power Sources 86 (2000) 423–431.

[8] C.W. Tanner, K.Z. Fung, A.V. Virkar, The effect of porous composite electrode structure on solid oxide fuel cell performance, I. Theoretical analysis, J. Electrochem. Soc. 144 (1997) 21–30.

[9] A. McDougall, Fuel Cells, MacMillan Press, London, 1976.

[10] A.V. Virkar, J. Chen, C.W. Tanner, J.-W. Kim, The role of electrode microstructure on activation and concentration polarizations in solid oxide fuel cells, Solid State Ionics 131 (2000) 189–198.

[11] J.-W. Kim, A.V. Virkar, K.-Z. Fung, K. Mehta, S. Singhal, Polarization effects in intermediate temperature, anode-supported solid oxide fuel cells, J. Electrochem. Soc. 146 (1999) 69–78.

[12] P. Costamagna, P. Costa, V. Antonucci, Micro-modelling of solid oxide fuel cell electrodes, Electrochim. Acta 43 (1998) 375–394.

[13] P. Costamagna, P. Costa, E. Arato, Some more considerations on the optimization of cermets solid oxide fuel cell electrodes, Electrochim. Acta 43 (1998) 967–972.

[14] S.H. Chan, Z.T. Xia, Anode micro model of solid oxide fuel cell, J. Electrochem. Soc. 148 (2001) A388–A394.

[15] S.H. Chan, X.J. Chen, K.A. Khor, Cathode micromodel of solid oxide fuel cell, J. Electrochem. Soc. 151 (2004) A164–A172.

[16] J.H. Nam, D.H. Jeon, A comprehensive micro-scale model for transport and reaction in intermediate temperature solid oxide fuel cells, Electrochim. Acta 51 (2006) 3446–3460.

[17] Y.X. Shi, N.S. Cai, A general mechanistic model of solid oxide fuel cell, Tsinghua Sci. Technol. 11 (2006) 701–711.

[18] K.P. Recknagle, R.E. Williford, L.A. Chick, D.R. Rector, Three-dimensional thermo-fluid electrochemical modeling of planar SOFC stacks, J. Power Sources 113 (2003) 109–114.

[19] H. Yakabe, T. Ogiwara, M. Hishinuma, I. Yasuda, 3-D model calculation for planar SOFC, J. Power Sources 102 (2001) 144–154.

[20] T. Nishino, H. Iwai, K. Suzuki, Comprehensive numerical modeling and analysis of a cell-based indirect internal reforming tubular SOFC, J. Fuel Cell Sci. Technol. 3 (2006) 33–44.

[21] J. Yuan, B. Sunden, Analysis of chemically reacting transport phenomena in an anode duct of intermediate temperature SOFCs, J. Fuel Cell Sci. Technol. 3 (2006) 89–98.

[22] N. Autissier, D. Larrain, J. Van herle, D. Favrat, CFD simulation tool for solid oxide fuel cells, J. Power Sources 131 (2004) 313–319.

[23] H. Yakabe, T. Sakurai, 3D simulation on current path in planar SOFCs, Solid State Ionics 174 (2004) 295–302.

[24] J. Fleig, Solid oxide fuel cell cathodes: polarization mechanisms and modeling of the electrochemical performance, Annu. Rev. Mater. Res. 33 (2003) 361–382.

[25] Y.X. Shi, N.S. Cai, C. Li, Numerical modeling of an anode-supported SOFC button cell considering anodic surface diffusion, J. Power Sources 164 (2007) 639–648.

[26] P. Costamagna, K. Honegger, Modeling of solid oxide heat exchanger integrated stacks and simulation at high fuel utilization, J. Electrochem. Soc. 45 (1998) 3995–4007.

[27] S. Nagata, A. Momma, T. Kato, Y. Kasuga, Numerical analysis of output characteristics of tubular SOFC with internal reformer, J. Power Sources 101 (2001) 60–71.

[28] F. Andriani, N. Walsh, Physical properties and textural parameters of calcaronitic rocks: qualitative and quantitative evaluations, Eng. Geol. 67 (2002) 5–15.

[29] P. Francus, An image-analysis technique to measure grain-size variation in thin sections of soft clastic sediments, Sediment. Geol. 121 (1998) 289–298.

[30] R.J. Braun, Optimal design and operation of solid oxide fuel cell systems for small-scale stationary applications, Ph.D. Thesis, University of Wisconsin, Madison, USA, 2002, pp. 109–111.